Nuclear Inst. and Methods in Physics Research, A 987 (2021) 164741

Contents lists available at ScienceDirect

Nuclear Inst. and Methods in Physics Research, A

journal homepage: www.elsevier.com/locate/nima

Analysis of the first magnetic results of the PSI APPLE X undulators in elliptical polarisation

Xiaoyang Liang [a,b,*], Marco Calvi [a], Marie-Emmanuelle Couprie [b], Romain Ganter [a], Christoph Kittel [a,c], Nicholas Sammut [c], Thomas Schmidt [a], Mathieu Valléau [b], Kai Zhang [a]

[a] Paul Scherrer Institut, Forschungsstrasse 111, 5232 Villigen PSI, Switzerland
[b] Synchrotron SOLEIL, L'Orme des Merisiers, Saint-Aubin - BP 48, 91192 Gif-sur-Yvette CEDEX, France
[c] Department of Microelectronics and Nanoelectronics, Faculty of Information and Communication Technology, University of Malta, Msida MSD2080, Malta

ARTICLE INFO

Keywords:
Soft X-ray
Elliptically polarised undulator
APPLE X undulator
Magnetic susceptibility

ABSTRACT

The new APPLE X undulators are novel elliptically-polarised undulators, which have a highly symmetric geometry. Theoretically, all the elliptical polarisation states are expected to have the same deflection parameter if the magnetic and geometrical errors are negligible. Nonetheless, the magnetic measurements of the first ten APPLE X undulators performed at Paul Scherrer Institut (PSI) contradicted this simple statement and numerical simulations were required to understand and validate the results. After the valuation of the magnetic-force induced mechanical deformations of the undulator frame, the central role played by the magnetic susceptibility χ was investigated. The simulation results indicate that the impact of different magnet types in the Halbach array, the *anisotropic* properties, and the choice of shaped field radial magnets are critical for the achieved magnetic field. The numerical results are compared with the measurement data.

0. Introduction

The second beamline of the SwissFEL [1] project at the Paul Scherrer Institut (PSI), Athos [2], is designed for Soft X-rays and is equipped with APPLE X undulators [3]. This new undulator design is part of a common effort in the Synchrotron light source community, well documented by these publications [4–10] which cover two decades of innovation.

Ten PSI APPLE X units have been magnetically tested following this procedure: 1. Alignment of the undulator on the measurement bench to probe the magnetic axis. 2. Optimisation of the phase error and of the trajectory. 3. Magnetic characterisation. The last step is used to evaluate the performance and to predict the behaviour of the undulators after their installation in the beamline, which requires a development of analytical models to summarise the large amount of data. An interpolation of the data is also a possible approach but physical models have been preferred to help the critical evaluation of the experimental results. In an APPLE type undulator the *parallel operational mode*, where two diagonal magnetic rows are shifted along the undulator axis against the lasting two rows, controls the elliptical polarisation states. The model detailed in [11] predicts that all elliptical polarisation states have the same deflection parameter, K, defined in the equation below,

$$K = \frac{eB\lambda_u}{2\pi mc} = \kappa B, \tag{1}$$

where B is the magnetic strength, λ_u the undulator period length, e and m the charge and the mass of the electron respectively and c the speed of light. Nevertheless, the experimental results contradict the above conjecture: in the example of Fig. 1, the measurements of K are plotted as a function of the parallel phase shift,

$$\phi_p = \frac{2\pi\Delta z}{\lambda_u}, \tag{2}$$

where Δz is the difference of the position along the undulator axis of two diagonal rows with respect to the other two, see Fig. 2. For convenience's sake, the peak observed in circular polarisation is defined as:

$$\Delta K_C = K_C - (K_{LH} + K_{LV})/2, \tag{3}$$

where $K_{C,LH,LV}$ are the K in Circular, Linear Horizontal and Linear Vertical polarisation states respectively. Besides, the consistent behaviour of the first ten APPLE X units tested up to now suggests an underlying physical mechanism.

This is the first time that this effect is visible and documented in a series production, probably because the large asymmetry between the horizontal and vertical components of the magnetic field dominates in previous APPLE (I, II or III) undulators. A similar example was reported in [12], where a 0.3 m long fix gap Delta undulator prototype presented a negative $\Delta K_C/K$ of about −0.9%.

* Corresponding author at: Paul Scherrer Institut, Forschungsstrasse 111, 5232 Villigen PSI, Switzerland.
E-mail address: xiaoyang.liang@psi.ch (X. Liang).

https://doi.org/10.1016/j.nima.2020.164741
Received 11 June 2020; Received in revised form 10 September 2020; Accepted 5 October 2020
Available online 16 October 2020

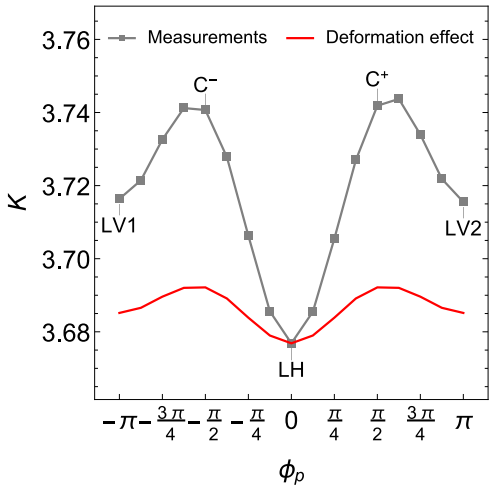

Fig. 1. An example of the measurements for deflection parameter K (measured and calculated with Eq. (11)) in *parallel operational mode*. The linear vertical polarisation states (LV1 and LV2), the horizontal polarisation state (LH) and the two circular, left and right handed, polarisation states (C^+ and C^-) are marked for an easy identification respectively. Three of their geometries are schematically presented in Fig. 2. The curve in red solid line is the calculated effect of the mechanical deformation. On average among the different modules, the deformation accounts for about a quarter of the measured effect on K_C and one tenth of the difference between K_{LH} and K_{LV}.

As a preliminary assessment, a simulation study of the mechanical deformation of the undulator support structure due to the magnetic forces has been carried out and validated against with mechanical measurements performed directly on the magnets. The corresponding changes on K are calculated and presented in Fig. 1 for an easy comparison. This effect accounts for about one quarter of the measured average peak (average of the different models) and for one tenth of the average asymmetry between LH and LV.

Consequently, the main part of this work is focused on the peculiar magnetic structure of the PSI APPLE X undulator. First, the magnets which form the Halbach array have different remanence and permeability: the radial units are made of a grade of Sm_2Co_{17} material while the axial ones are made of $SmCo_5$. In this regard, we will refer to this type of mixed magnetic array as *zebra*-type in this article. Second, the radial magnets are produced with the so-called shaped field technique [3,13], with which the powders are oriented towards a target point using a non uniform magnetic field. This is different from the regular uniform orientation of the magnetic powders during the pressing process achieved with a uniform pulsed magnetic field. In this application, the powders are oriented towards the centre of the undulator axis in order to enhance the magnetic field. With this technology, an increase of the field strength between 5% and 10% is expected.

In the following section, the analytical model presented in [11] is extended to the full Fourier spectrum and the associated method to evaluate K will then be applied to different numerical models of increasing complexity.

1. Analytical model

The magnetic field of an APPLE type undulator can be expressed as the sum of the field generated by each row [11,14]. Limiting the investigation to the on-axis field, this statement can be summarised through the following equation:

$$\mathbf{B}(z) = \sum_{n=1}^{4} \mathbf{B}_n \left(z - z_n\right), \tag{4}$$

where z is the spatial coordinate along the magnetic axis. Eq. (4) can be expressed as a function of one of the four rows using the symmetries $\mathbf{R}_n$ of the cross section of the APPLE undulator,

$$\mathbf{B}(z) = \sum_{n=1}^{4} \mathbf{R}_n \cdot \mathbf{B}_1 \left(z - z_n\right). \tag{5}$$

The above expression has a simpler formulation in the Fourier domain (denoted with a hat, $\hat{}$):

$$\hat{\mathbf{B}} = \sum_{n=1}^{4} \exp(i\phi_n)\mathbf{R}_n \cdot \hat{\mathbf{B}}_1 \tag{6}$$

and $\hat{\mathbf{B}}_1$, the on-axis magnetic field generated by one of the magnetic row (by convention, the one of the first quadrant), can be explicitly written as the sum of its harmonics [14]. Eq. (6) becomes:

$$\hat{\mathbf{B}} = \sum_{h} \sum_{n=1}^{4} \exp(ih\phi_n)\mathbf{R}_n \cdot \hat{\mathbf{B}}_{1h}, \tag{7}$$

where the field expression of each harmonic, $\hat{\mathbf{B}}_h$, can be finally written as,

$$\hat{\mathbf{B}}_h = \sum_{n=1}^{4} \exp(ih\phi_n)\mathbf{R}_n \cdot \hat{\mathbf{B}}_{1h}. \tag{8}$$

The effective deflection parameter to be used in the fundamental undulator equation [15], hereafter

$$\lambda = \frac{\lambda_u}{2\gamma^2}\left(1 + \frac{K^2}{2}\right), \tag{9}$$

is given by

$$K^2 = \sum_{h} \mathbf{K}_h \cdot \mathbf{K}_h^*, \tag{10}$$

where

$$\mathbf{K}_h = \frac{\kappa}{h}\hat{\mathbf{B}}_h$$

A demonstration of Eq. (10) for a generic APPLE geometry is presented in Appendix. This firstly provides a very general and accurate formula used in this paper for the evaluation of K out of measurements and simulations as a function of the Fourier components of the magnetic field, both in x- and y-axes,

$$K = \kappa \sqrt{\sum_{h} \left(\frac{\hat{B}_{xh}}{h}\right)^2 + \left(\frac{\hat{B}_{yh}}{h}\right)^2} \tag{11}$$

Secondly it also provides the following prediction for the case of an APPLE X,

$$K = 4\kappa \sqrt{\sum_{h} \left(\frac{\hat{B}_h}{h}\right)^2} \tag{12}$$

where $\hat{B}_h = \hat{B}_{1h} = \hat{B}_{1xh} = \hat{B}_{1yh}$ represents theoretically the horizontal or vertical magnetic strength of one array. Because of the symmetry of an ideal APPLE X undulator, the horizontal and the vertical magnetic field components are equal. With an opportune choice of the initial phase, they are also real numbers. Eq. (12) predicts that the K should be independent of the phase of the parallel shift ϕ_p and the presence of high order harmonics slightly only changes its absolute value.

As a practical tool for the data analysis, it is convenient to estimate K, this time only for the first harmonic ($h = 1$) when $\hat{B}_{1x} - \hat{B}_{1y} = \delta B$, where δB is small but not zero. This is usually the case in a real device and in particular in the APPLE X undulators where an equivalent angle deviation (with respect to the ideal 45°) is estimated to be less than a few degrees. Under the above condition, Eq. (12) can be written as follows,

$$K \sim K_{LH} + \Delta K_{LV} \sin^2(\phi_p/2), \tag{13}$$

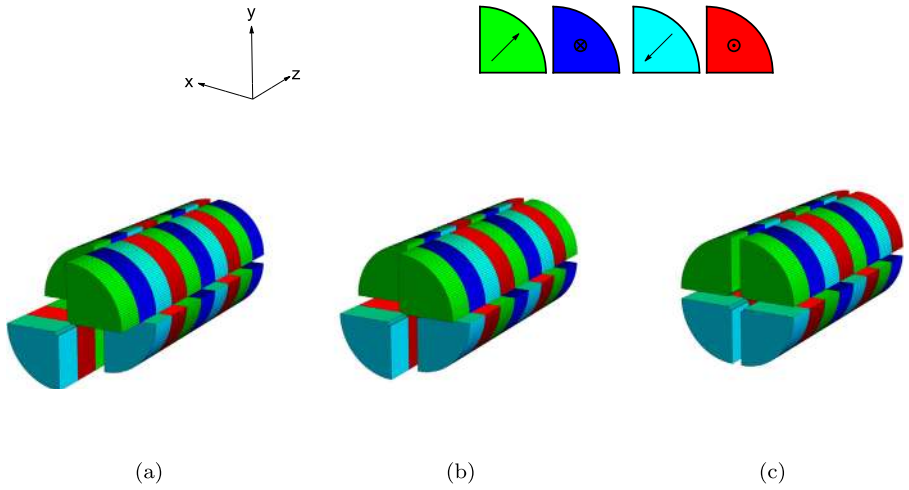

Fig. 2. 3D model of the magnetic arrays in the parallel undulator operational mode, where three elliptical polarisation states are presented: (a) Linear Vertical (LV1), where $\phi_p = -\pi$. The rows are shifted with half the undulator period. (b) Circular minus (C^-) with $\phi_p = -\pi/2$. (c) Linear Horizontal (LH) whose ϕ_p is 0. In this state, there is no shift between the magnetic arrays.

where K_{LH} is K in Linear Horizontal polarisation, while ΔK_{LV} is its difference with respect to K in Linear Vertical.

An example of popular K-approximation is to evaluate it directly using the maximum value of the magnetic field profile. This is the typical textbook approximation [15], valid under the assumption of a perfect sinusoidal magnetic field profile. On a real undulator, which has small but not negligible harmonics, this approximation produces a qualitatively different trend if used to estimate the changes of K in elliptical polarisation: it does not predict a constant value like equation (12) but a function of ϕ_p similar to our experimental results. It is possible to produce an analytical expression of K based on the maximum value of the magnetic field profile using the Fourier formalism. The expression truncated for the sake of simplicity to the third harmonic becomes:

$$K = 4\kappa\sqrt{\hat{B}_1^2 - 2\hat{B}_1\hat{B}_3\cos^2\phi_p + \hat{B}_3^2}\,, \tag{14}$$

where K changes with ϕ_p and has a maximum or a minimum in circular polarisation, depending on the sign of $\hat{B}_3$. Eq. (14) can be further manipulated by assuming that $b_3 = \hat{B}_3/\hat{B}_1 \ll 1$ which results in the variation of K with respect to ϕ_p reducing to

$$\delta K \sim b_3 \sin^2\phi_p \tag{15}$$

and by analogy the equation is extended to high order corrections in a Fourier fashion

$$\delta K \sim \sum_{n>0} \delta_n \sin^2 n\phi_p\,. \tag{16}$$

We would like to emphasize that this is just an analogy with no physical meaning, and it is used later as a practical tool for fitting the experimental data. A detailed analysis of the harmonics as a function of ϕ_p was not carried out in this preliminary work and we reserve the possibility to propose a second manuscript in case that this study brings further light into this effect.

By looking further into the details of the material properties (in particular the large *anisotropic* properties introduced by the *zebra*-type configuration), we found that it was possible to explain the phenomenon(ΔK). Indeed, only numerical simulations can be used to investigate the effect of a magnetic susceptibility larger than zero, where the assumption of simple superposition of the magnetic fields produced by different sources does not apply any longer.

Table 1
Magnetic material simulated in RADIA 4.31.

Magnetic material	$\chi_{\parallel}$ –	$\chi_{\perp}$ –	B_r T	Comment	Type in *zebra*
M_{i1}	0.00	0.00	1.0	*Isotropic*	Axial
M_{i2}	0.14	0.14	1.0	*Isotropic*	Radial
M_{a1}	0.00	0.14	1.0	*Anisotropic*	Radial
M_{a2}	0.14	0.00	1.0	*Anisotropic*	Radial
$SmCo_5$	0.01	0.04	0.94	–	Axial
Sm_2Co_{17}	0.04	0.14	1.1	–	Radial

2. Numerical models

2.1. Configurations and settings of the numerical simulation

The numerical simulations were carried out within the Wolfram Mathematica© environment using the code RADIA 4.31. The method used in RADIA belongs to the category of boundary Integral Methods [16,17]. Volume objects are created and material properties are applied to them. Each object can be subdivided into a number of smaller objects for which the magnetization is estimated with an interactive algorithm.

Two undulator geometries have been used for this numerical study: the first one, quite popular and simple to implement, later referred to as the *cubic* geometry is depicted in Fig. 3(a). The second geometry is called the *cylindrical* one and is depicted in Fig. 3(b). The *cubic* geometry is used to start the step-by-step investigation. The first set of simulations was done assuming a uniform magnetisation of the building blocks of the Halbach array, at the designed 45° angle. As for the *cylindrical* model, on one hand, it is closer to the actual PSI APPLE X geometry, whilst on the other hand it makes the implementation of the shaped field more natural in the simulations. This is because the magnetisation of each element corresponds, in good approximation, to the orientation of the radial mesh, as shown in Fig. 3(d).

In Table 1, the material parameters used for the simulations are listed. The two lines at the bottom correspond to commercial materials and their susceptibilities are measured by the magnet manufacturer. In this context they are used for a direct quantitative comparison with the measurement results. In contrast, the first four rows of the table (M) do not necessarily correspond to any existing materials and they are solely designed to conduct a systematic study of the effect of the susceptibility. In order to correctly account for the properties of those magnetic materials, the susceptibility is sorted in two types: the susceptibility

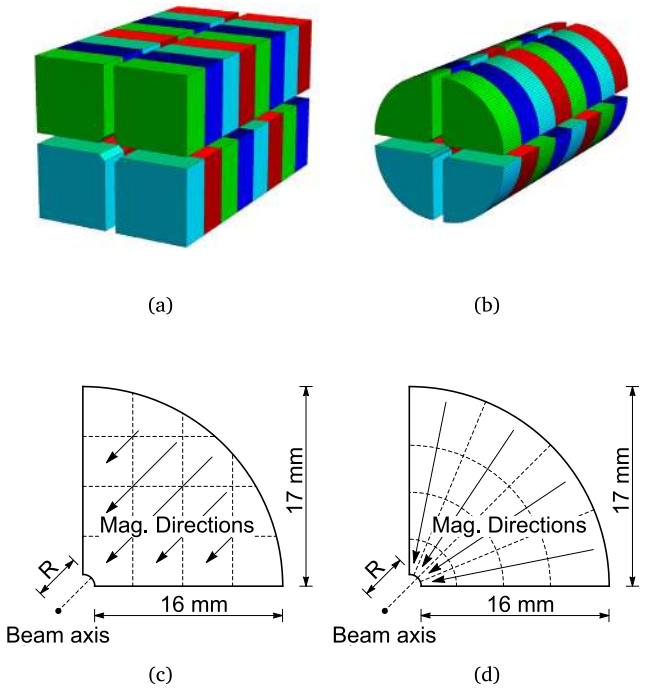

Fig. 3. (a) 3D Model simulation with RADIA 4.31: Two undulator periods are presented with *cubic* geometry. (b) 3D model with *cylindrical* geometry. (c) 2D cross section schema of magnets in *cylindrical* geometry. The dashed lines represent the mesh of the subdivision for the magnets in the simulation. The distance between the electron beam axis (undulator central axis) and the magnet is defined as gap radius R. (d) The shaped field technique is applied, where the magnetisation direction are not homogeneous 45° but varying and pointing to the beam axis.

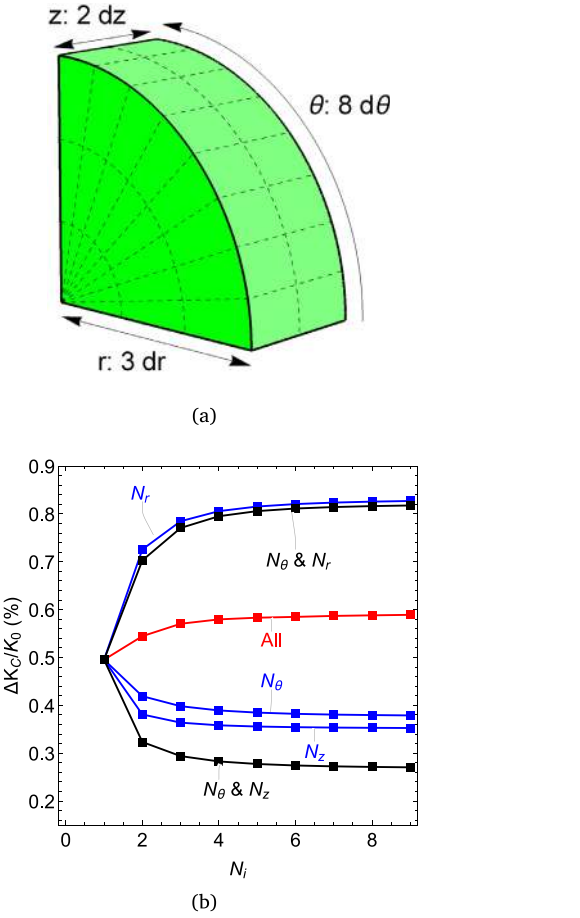

Fig. 4. (a) 3D schema of an example with subdivision $\{3, 8, 2\}$. (b) In the case of *zebra*-type structure with mixed material $SmCo_5$(axial) and Sm_2Co_{17}(radial) at $R = 3.25$ mm, the relative ΔK_C (see Eq. (3)) compared with K_0 (K_{LH} at minimum gap radius) versus subdivisions. Cylindrical geometry and shaped field simulation were applied. (For interpretation of the references to colour in this figure legend, the reader is referred to the web version of this article.)

parallel to the magnetisation axis ($\chi_\parallel$) and the one perpendicular to the magnetisation axis ($\chi_\perp$). The materials with $\chi_\parallel = \chi_\perp$ in this context are called *isotropic* whilst the others are called *anisotropic*. To avoid ambiguity, all magnetic materials used in undulator applications are produced by orienting their constituent powders to increase the remnant magnetisation, or in short, the *remanence* (B_r). This creates a preferential magnetisation direction and thus they are all commonly referred to as anisotropic magnets. However, in this paper, *anisotropic* magnets refer to magnets with susceptibility $\chi_\parallel \neq \chi_\perp$.

The mesh size is an important factor to correctly untangle the effect we are investigating. A coarse mesh is usually enough in an APPLE undulator to catch the main effect and has both a quantitative (at a level of 10^{-2}) and qualitative description of the magnetic field, because of the low magnetic susceptibility of permanent magnets. This is not the case for undulators equipped with iron poles (like in the case of in-vacuum undulators), because the large change of susceptibility between permanent magnets and iron requires more degrees of freedom to solve the Maxwell equations accurately. As the magnetic flux lines bend with smaller radius, it requires finer meshes than for a regular APPLE type structure. A similar effect occurs for *zebra*-types where a tiny but abrupt change of susceptibility happens between two neighbouring magnets and hence a finer mesh is required to describe this small but intriguing stationary point in circular polarisation.

2.2. Numerical convergence study

Since the effect under investigation (ΔK_C) is quite small (at a level of one percent), even if not at all negligible to predict the resonance of an undulator (Eq. (9)), a detailed study of the numerical convergence as a function of the mesh size of subdivision in RADIA had to be carried out.

An example of the 3D mesh for *cylindrical* geometry is presented in Fig. 4(a), where the magnet is subdivided in the three directions: r, θ and z.

In order to check the effect of mesh size, different simulations were done by modifying the subdivisions (N_i) in one, two or in all three directions, Fig. 4(b). When varying one or two parameters, the remaining N_i are kept equal to one. Increasing the number of subdivisions converges quickly ($N_i > 5$) to a reasonable stable value. Varying the subdivision of only one or two directions also converges but to an erroneous value. Only when all three N_i parameters are changed simultaneously (see red line in Fig. 4(b)), does the simulation gives a consistent solution to the problem. This study demonstrates the convergence; it gives the possibility to select a trade off between the required accuracy and computational time and highlights the great dependence of this effect from chosen mesh. As an example, the computation time for the subdivision $\{10, 10, 10\}$ is more than 3 h for only one K point. The results presented in Fig. 4(b) show a spread of almost a factor of 3 in the amplitude of the ΔK_C when varying only one or two subdivision parameters, N_i.

2.3. Simulation results and interpretation

Two sets of simulation results are presented: the *cubic* geometry without shaped field in Fig. 5 and the *cylindrical* geometry with shaped

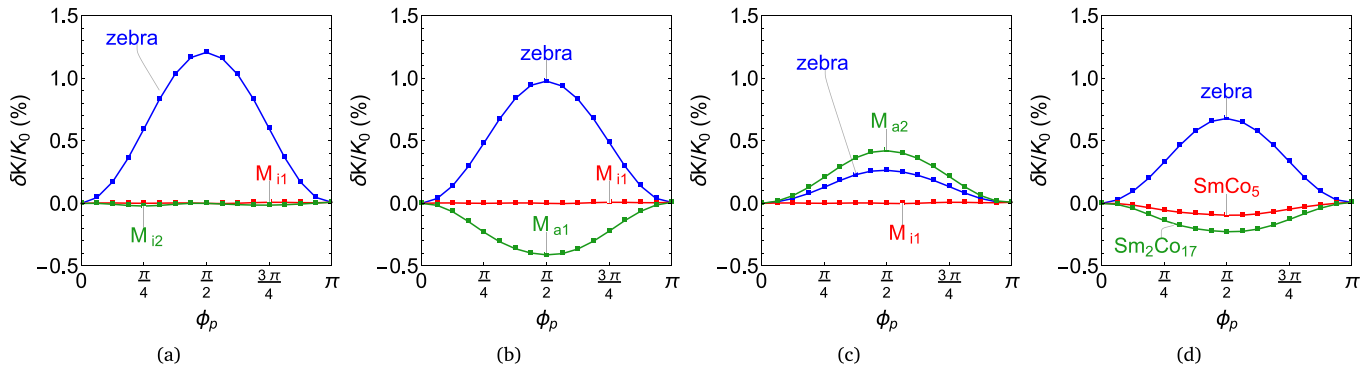

Fig. 5. The K variation in elliptical polarisation states (*parallel operational mode*) is evaluated for three different row arrangements of magnets, the following colour and material convention of the curves is kept also for Fig. 6: Red: Normal Halbach structure constructed only with the material labelled. Green: Halbach structure with the material labelled. Blue: *Zebra*-type Halbach structure, where the **axial** magnets are built with the material labelled in **red** colour while the **radial** magnets are built with the one in **green**. (a) M_{i1}: $\chi_\parallel = 0$, $\chi_\perp = 0$; M_{i2}: $\chi_\parallel = 0.14$, $\chi_\perp = 0.14$. (b) M_{i1}: $\chi_\parallel = 0$, $\chi_\perp = 0$; M_{a1}: $\chi_\parallel = 0$, $\chi_\perp = 0.14$. (c) M_{i1}: $\chi_\parallel = 0$, $\chi_\perp = 0$; M_{a2}: $\chi_\parallel = 0.14$, $\chi_\perp = 0$. (d) $SmCo_5$: $\chi_\parallel = 0.01$, $\chi_\perp = 0.04$; Sm_2Co_{17}: $\chi_\parallel = 0.04$, $\chi_\perp = 0.14$. (For interpretation of the references to colour in this figure legend, the reader is referred to the web version of this article.)

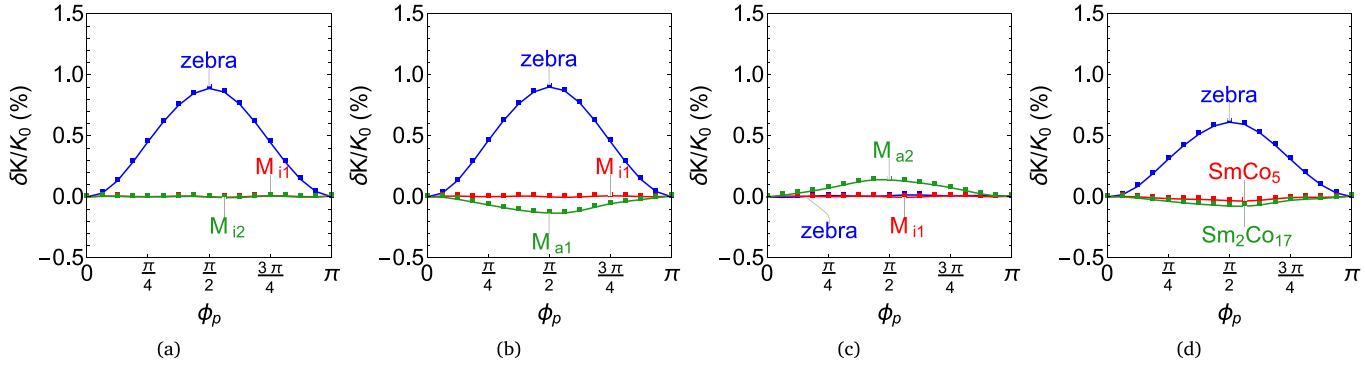

Fig. 6. The simulations presented in Fig. 5 are now repeated for the *cylindrical* geometry with shaped field. The other parameters remain the same. As a reminder: Blue: *Zebra*-type Halbach structure, where the **axial** magnets are built with the material labelled in **red** colour while the **radial** magnets are built with the one in **green**. (a) M_{i1}: $\chi_\parallel = 0$, $\chi_\perp = 0$; M_{i2}: $\chi_\parallel = 0.14$, $\chi_\perp = 0.14$. (b) M_{i1}: $\chi_\parallel = 0$, $\chi_\perp = 0$; M_{a1}: $\chi_\parallel = 0$, $\chi_\perp = 0.14$. (c) M_{i1}: $\chi_\parallel = 0$, $\chi_\perp = 0$; M_{a2}: $\chi_\parallel = 0.14$, $\chi_\perp = 0$. (d) $SmCo_5$: $\chi_\parallel = 0.01$, $\chi_\perp = 0.04$; Sm_2Co_{17}: $\chi_\parallel = 0.04$, $\chi_\perp = 0.14$. (For interpretation of the references to colour in this figure legend, the reader is referred to the web version of this article.)

field in Fig. 6. In the analysis, only the relative variation of the deflection parameter K is presented in the following form:

$$\delta K/K_0 = \frac{K(\phi_p) - K(0)}{K_0}$$

where K_0 is the K at minimum radius $R = 3.25$ mm in Linear Horizontal polarisation. $K(\phi_p)$ is the actual K for a given parallel shift. In this first numerical investigation, the $K(\phi_p)$ is estimated at the minimum radius as well.

2.3.1. Cubic geometry without shaped field

The results of these first numerical calculations are presented in Fig. 5. The curves of *isotropic* materials M_{i1} (red) and the M_{i2} (green) of Fig. 5(a) are for any practical purpose identically flat, even if the susceptibility of the latter one is not zero. In contrast, the *zebra*-type (blue) which is composed of axial magnets with M_{i1} and radial magnets with M_{i2} produces a local peak in circular polarisation (C) of about 1.2% relative to Linear Horizontal (or Vertical) polarisation state.

In Fig. 5(b), the green curve is the result of a Halbach structure with *anisotropic* material M_{a1}, where a local minimum is now well pronounced in circular polarisation. This was observed for instance in the previously cited Delta prototype [12]. The *zebra*-type made with radial magnets M_{a1} and axial magnets M_{i1}, generates a local maximum. Although it is less pronounced than in Fig. 5(a), the amplitude of this local maximum of the *zebra*-type structure (blue) is larger than the one of the local minimum in the case of the Halbach array with M_{a1} (green).

In Fig. 5(c), the green curve is calculated with the other *anisotropic* magnets M_{a2}, with which a local but small maximum is generated, whereas the *zebra*-type presents an even smaller local maximum.

Also in the case of the simulated materials $SmCo_5$ and Sm_2Co_{17}, the K variation presents a pronounced local maximum (blue curve in Fig. 5(d)).

The above simulation results confirm that the non-linearities ($\chi > 0$) do not produce alone the observed effect in the APPLE X undulator (M_{i2} in Fig. 5(a)). This example shows clearly that the key ingredient which generates the local K maximum is not the presence of high order harmonics or the larger susceptibility, but the inhomogeneity of the magnetic structure, in this example due to the *zebra*-type Halbach arrangement.

Nevertheless, the effect simulated using our best knowledge of the material parameters, does not match alone quantitatively the experimental observations.

2.3.2. Cylindrical geometry without and with shaped field

The qualitative agreement of the above results instigates the possibility of a more quantitative prediction of the experiments if more details are taken into account. Firstly, we implement cylindrical magnets in the simulations which fit better the designed geometry of the

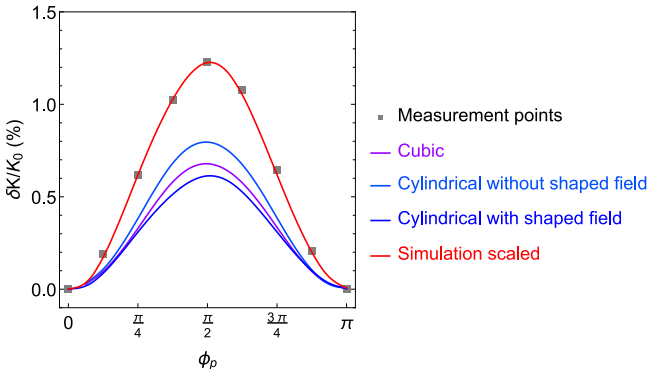

Fig. 7. Comparison of the *zebra* Halbach simulations using the same material setting (axial: $SmCo_5$, radial: Sm_2Co_{17}) but using three different geometries. In order to compare directly the curve shape of the simulation results with the measurement points (grey markers), one set of simulation is multiplied with a coefficient in red solid line. (For interpretation of the references to colour in this figure legend, the reader is referred to the web version of this article.)

PSI APPLE X magnets. Secondly, we implement the shaped field of the radial magnets, as sketched in Fig. 3(d). The *cylindrical* geometry without shaped field confirms the same qualitative, previously observed behaviour by the *cubic* geometry with negligible quantitative differences. Furthermore, the quantitative differences due to the geometry change (from *cubic* to *cylindrical*) were not large enough to require a new set of plots. Therefore, only the complete set of simulations with shaped field magnets is reported.

The details of the simulation using the *cylindrical* geometry with shaped field are presented in Fig. 6. The first evidence, comparing to the non shaped field cases, is the reduction of the anisotropy effect. The single *anisotropic* material (green curves) shows an almost negligible peak (either a maximum or a minimum) in Fig. 6(c). Intuitively, the shaped field spoils the concept of parallel and perpendicular susceptibility with respect to the Cartesian reference frame and it is not surprising that this minimises its impact.

However, after using more realistic simulation parameters the discrepancy between the simulation and the measurements of ΔK_C increased instead of decreasing. In Fig. 7, this effect is presented for three *zebra*-types: *cubic*, *cylindrical* without shaped field and *cylindrical* with shaped field.

2.3.3. Susceptibility study

The different amplitudes of the curves in Figs. 5 and 6 are strongly correlated to the susceptibility values of the magnetic materials in Table 1. This indicates a simple relation between ΔK_C and the susceptibility. Therefore, a systematic study was made and it is presented in Fig. 8. In Fig. 8(a) a *zebra*-type is analysed and the peak is plotted as a function of the difference in susceptibility, $\Delta\chi$, between the radial and the axial magnets. The three curves respectively represent the effect of the perpendicular susceptibility difference, $\Delta\chi_\perp$, the parallel susceptibility difference, $\Delta\chi_\parallel$, and both together, $\Delta\chi_\perp$&$\Delta\chi_\parallel$. The dominant effect for a *zebra*-type undulator is $\Delta\chi_\perp$, while the effect of the parallel susceptibility difference is negligible. The results for a regular Halbach array made of one magnetic material are presented in Fig. 8(b). When the material is *isotropic* $\chi_\perp = \chi_\parallel$, there is no peak as already observed in the few examples above. In contrast, the peak decreases at increasing $\chi_\perp$(when $\chi_\parallel = 0$) while it increases at increasing $\chi_\parallel$ (when $\chi_\perp = 0$). In the range explored, the dependence of ΔK_C with respect to the susceptibility is, for any practical purpose, linear and its slope can be used to predict the effect without time consuming simulations.

2.3.4. Final remark on the simulation results

A detailed analysis of the elliptical polarisation states of an APPLE X undulator has been carried out with the numerical code RADIA. Before concluding this section, it is mandatory to look once at the absolute value of K, see Fig. 9 for an example of a *zebra*-type undulator. As expected, the field strength in an undulator decreases with the rise of susceptibility, so the peak observed in the *zebra*-type is due to a lower decrease in field strength in circular polarisation which is less than in linear polarisations. In conclusion, ΔK_C is not an increase of the field at an increasing susceptibility but only a more moderate decrease of the field with respect to the other elliptical polarisation states.

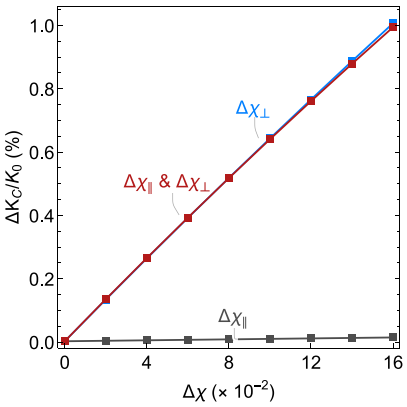

(a) *zebra*-type Halbach structure

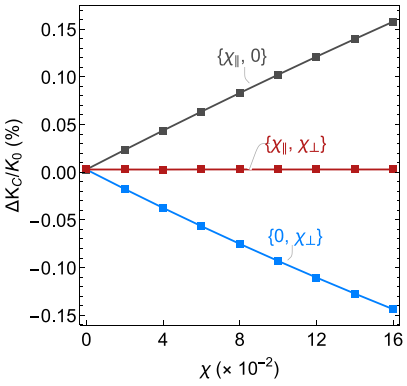

(b) Single material Halbach structure

Fig. 8. The relative ΔK_C with respect to K_{LH} at minimum gap as a function of $\Delta\chi$ or χ. Cylindrical geometry and shaped field are applied.

3. Magnetic measurements and data analysis

During the series production, all APPLE X undulators are magnetically tested in the PSI laboratories. As shown in Fig. 10, the newly developed electronics [18–20] for the read-out of the SENIS Hall S-type probe is used and integrated into a SAFALI bench [21,22]. Among a set of more than a thousand magnetic field profile acquisitions per undulator module, a subset is dedicated to the characterisation of the elliptical polarisation. A full shift of ϕ_p is systematically performed at several gaps: from LV1, C^-, LH, C^+ to LV2 (see Fig. 11(a)) with a total of 17 recorded K. Presently, five APPLE X units have been measured (including the prototype) and two main parameters have been extracted using the following procedure and by means of the equations described below.

First, the smooth transition between LH and LV is calculated with Eq. (13), using the measured value of K_{LH} and $K_{LV1\&2}$. This is then subtracted as a background, see Fig. 11(b). The residual values (δK)

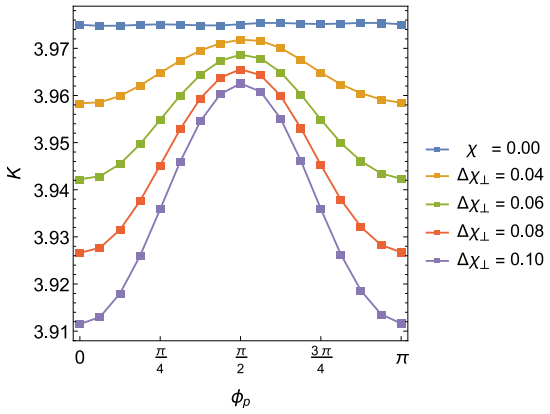

Fig. 9. The deflection parameter K as a function of the phase shift in *parallel operational mode* for a series of $\Delta\chi_\perp$ in *zebra* structure, where $\Delta\chi$ is the difference between the χ of radial magnets with respect to axial magnets.

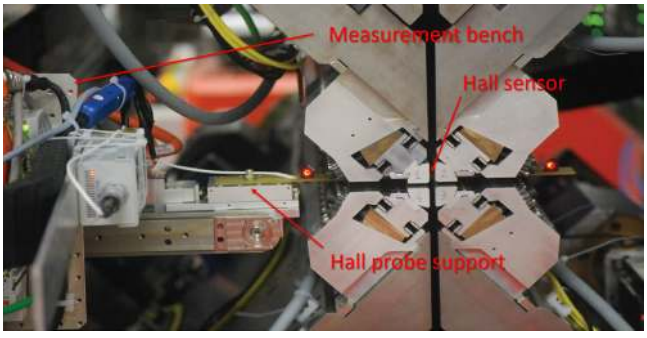

Fig. 10. A photo of the APPLE X cross section taken during the magnetic measurements at PSI laboratories. On the right hand side the four magnetic rows and on the left side the magnetic measurement bench guided by the two red laser spots, in a close loop SAFALI system. (For interpretation of the references to colour in this figure legend, the reader is referred to the web version of this article.)

are fitted with Eq. (16) truncated to the first two odd terms:

$$\delta K = \delta_1 \sin^2 \phi_p + \delta_3 \sin^2 3\phi_p. \tag{17}$$

The amplitude of the peak in circular polarisation is evaluated as $\Delta K_C = \delta_1 + \delta_3$. Eq. (17) describes changes of K across a full parallel shift with a relative accuracy well below 10^{-3} as shown in Fig. 11(d).

4. Systematic comparison between measurements and simulations

After presenting the data analysis method, the measurements are compared to the simulations. Fig. 12 shows ΔK_C versus gap for the first ten APPLE X modules, where the peaks in C^+ and C^- polarisation states are reported for comparison. The results of the most refined simulations are shown in a solid red line and are identical in both polarisation states as is expected by perfect symmetry. The effect of the mechanical deformation is presented in a solid blue line. Combining those two factors, namely the susceptibility and deformation, in the dashed red line, gives a better prediction of the experimental results. Moreover, the different decays of the two effects as a function of the radius, well describes the tails of the data, more exponential at small radii and more linear at larger ones.

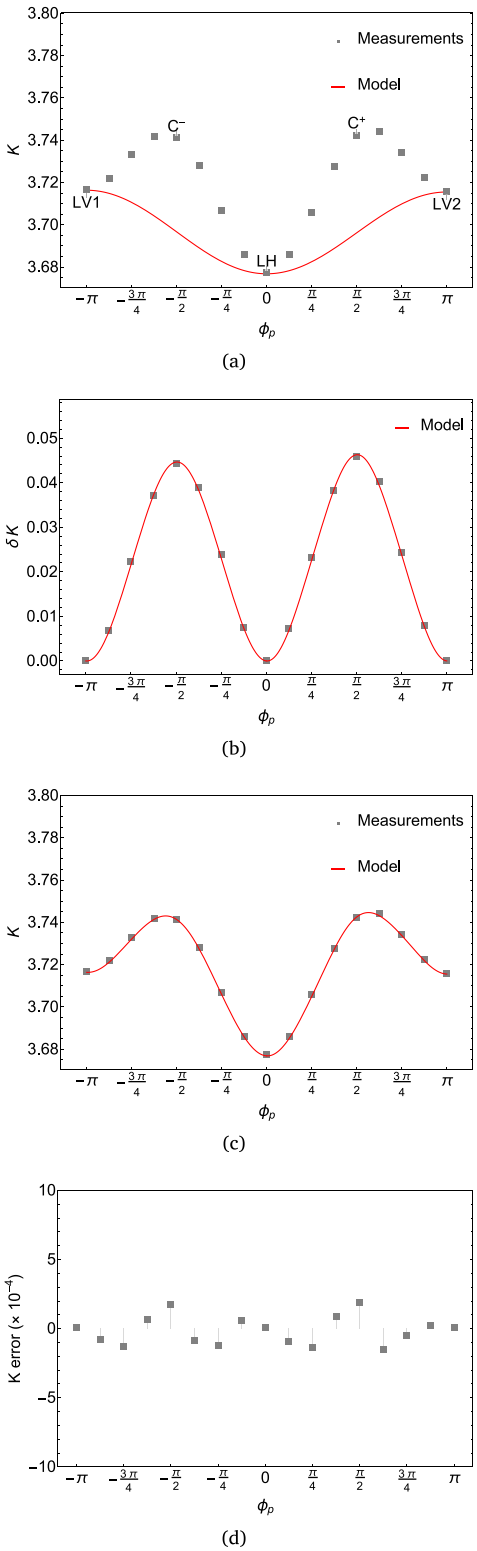

Fig. 11. The fitting procedures and performance of the example at minimum gap $R = 3.25$ mm: (a) With the fitting model using the Eq. (13), the asymmetry between the transition from LH to LV is subtracted. (b) After the subtraction, we fit the residual part using the model of Eq. (17). (c) Combining the models in (a) and (b), we obtain the final model for the measurements. (d) Relative error of the model in (c), compared with measurements data.

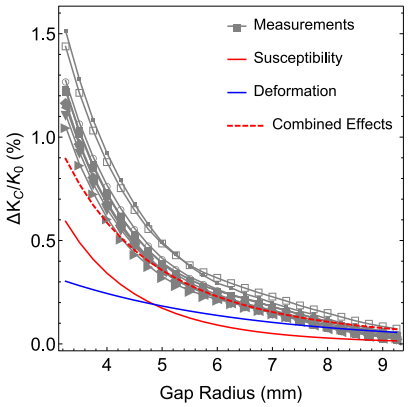

(a) Cases in C^- polarisation mode

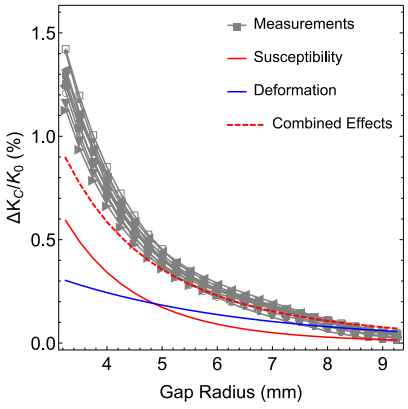

(b) Cases in C^+ polarisation mode

Fig. 12. The measurements of the ΔK_C as a function of the Gap Radius on the first ten APPLE X undulator units of the Athos beamline are presented together with the results of the simulations of a *zebra*-type *cylindrical* geometry combined with the effect of the mechanical deformation (red dashed line). The separate contributions of the susceptibility and deformation are presented respectively in the red and blue solid lines. (For interpretation of the references to colour in this figure legend, the reader is referred to the web version of this article.)

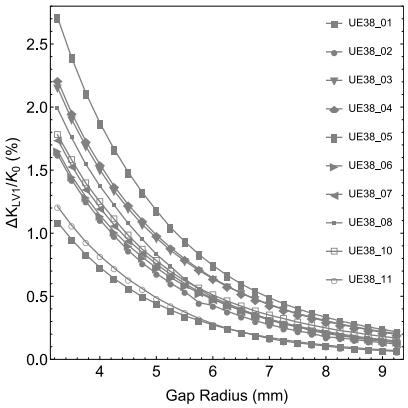

(a)

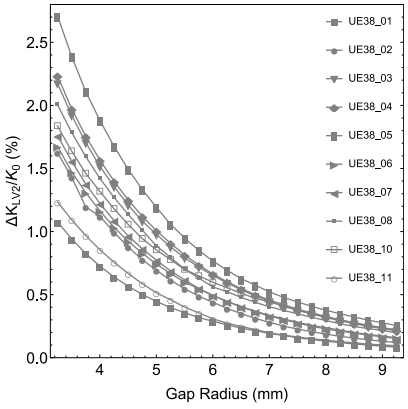

(b)

Fig. 13. The difference of K between LH and LV1 polarisation mode(left) and between LH and LV2 polarisation mode(right).

The experimental results show a spread among different undulator units and a small systematic difference between the two circular polarisation states: the peak in the C^+ is always lower than in C^-.

There is still a discrepancy between measurements and simulations. The latter still underestimate the real observed phenomenon of local K variations, ΔK_C. We have not identified additional effects which could explain it and we assume that a better knowledge of the magnetic and mechanical properties could explain the remaining gap between simulation results and measurement data. The consistency among different undulator modules is a clear sign that this effect is dominated by the design parameters (magnets and mechanical support frame), more than by the details of the assembling process.

In Fig. 13, the difference, ΔK_{LV}, between the K in linear horizontal (LH) and in vertical polarisations (both extremes of vertical polarisation, LV1 and LV2), are shown for the ten undulator units. The total spread among them is more than a factor of two (while $K_{LV1} \approx K_{LV2}$). This behaviour is clearly related to the specific details of each undulator assembly and cannot be predicted but only kept under control via a quality process. This difference can also be expressed as an equivalent magnetisation angle deviation from 45°, in this case always to one side (bend to the horizontal plane) and lower than 0.8°. The equivalent angle systematically decreases with increasing gap.

5. Conclusions

Our studies show that the details of the susceptibility of the magnets and the mechanical properties of the support frame structure of the PSI APPLE X undulators have to be carefully taken into account to correctly interpret and validate the experimental results. Understanding the *zebra*-type structure (alternating materials with different susceptibility in a Halbach structure) is essential to explain the presence of a local K-peak in the elliptical polarisation states. The more difference of the perpendicular susceptibility ($\chi_\perp$) value between the axial magnets and radial magnets, the larger is this effect.

The complexity of these types of structures cannot be easily untangled without numerical simulations. However, this study gives some simple instruments and ideas to interpret the results. This last aspect is crucial, especially when measuring complex undulator structures like those of the APPLE type. The presence of strong and highly inhomogeneous magnetic fields, like in circular polarisation, can generate spurious signals in a Hall probe due to the non-negligible planar effect [23]. Our magnetic bench is designed to be insensitive to this effect thanks to the spinning current technique. Nevertheless, these results, without a clear physical interpretation, may raise questions about the measurement quality and its reliability. Thus, we consider understanding the experimental results to be of paramount importance, even if only qualitatively, before trusting the output of our readout electronics blindly.

Although we did not achieve a quantitatively perfect agreement (within the spread of the production) between the simulations and the measurements, Eq. (17) fits accurately the data and it is now used to

feed the control system of the SwissFEL beamline in order to predict the deflection parameter when operated in elliptical polarisation state.

More generally, the analysis tools presented in this article are effectively used to steer the series production of complex APPLE undulators. They give simple parameters to verify if the production proceeds smoothly and in a reproducible fashion, and to detect if sudden and unwanted changes occur. This is true for the magnets, for their assembly and for the large mechanical support which holds their large magnetic forces and moves them precisely to change the magnetic configuration.

CRediT authorship contribution statement

Xiaoyang Liang: Software, Visualization, Methodology, Investigation, Formal analysis, Writing - original draft, Writing - review & editing. **Marco Calvi:** Conceptualization, Methodology, Writing - original draft, Validation, Writing - review & editing. **Marie-Emmanuelle Couprie:** Writing - review & editing, Funding acquisition, Project administration. **Romain Ganter:** Funding acquisition, Project administration. **Christoph Kittel:** Software, Writing - review & editing. **Nicholas Sammut:** Writing - review & editing, Validation. **Thomas Schmidt:** Supervision, Project administration. **Mathieu Valléau:** Software. **Kai Zhang:** Software.

Declaration of competing interest

The authors declare that they have no known competing financial interests or personal relationships that could have appeared to influence the work reported in this paper.

Acknowledgements

This work was carried out in the context of the Athos Project at PSI and we would like to acknowledge all people involved, specially the colleagues of the magnetic laboratories, M. Bruegger, R. Felder and S. Danner for their devotion to the magnetic measurements activities. The collaboration between SOLEIL and PSI, in the context of the LEAPS consortium, stimulated this scientific initiative supported by L. Patthey and Prof. L. Rivkin. The shaped field SmCo magnets for the Athos undulators have been realised in a fruitful collaboration between PSI and Arnold Magnetics, which has been supported by the Swiss Innovation Agency Innosuisse, Switzerland.

Appendix

A.1. Calculation of the deflection parameter taking into account the higher harmonics

The demonstration of the calculation for the undulator deflection parameter K from the magnetic field B [22] is presented in this appendix.

To describe the magnetic field we use the coordinate system of the electron beam trajectory (undulator axis) in accelerators: it composes a transverse plane (x, y) along with its longitudinal position z (see Fig. 2(a)). The horizontal and vertical components of the magnetic field are named respectively as B_x and B_y. We are starting from the equation of motion for relativistic electrons in a magnetic field in dependence of z:

$$\ddot{x}(z) = \frac{e}{\gamma mc} B_y(z) \tag{A.1}$$

$$\ddot{y}(z) = \frac{e}{\gamma mc} B_x(z). \tag{A.2}$$

The periodical magnetic fields are not purely sinusoidally distributed along the undulator axis. The equation describing the magnetic field can be expressed in a Fourier series. The different harmonic orders of the series are noted as h:

$$B_y(z) = \sum_h B_{yh} \cos\left(\frac{2\pi h}{\lambda_u} z\right) \tag{A.3}$$

$$B_x(z) = \sum_h B_{xh} \cos\left(\frac{2\pi h}{\lambda_u} z + \phi\right). \tag{A.4}$$

The constant ϕ in formula (A.4) represents the phase difference which can exist between these components. By inserting (A.3) into (A.1) and integrating (A.1) over z, we obtain:

$$\dot{x}(z) = \frac{\kappa}{\gamma} \sum_h b_{yh} \sin\left(\frac{2\pi h}{\lambda_u} z\right), \tag{A.5}$$

where κ and b_{yh} are defined as: $\kappa = \frac{e\lambda_u}{2\pi mc}$ and $b_{yh} = \frac{B_{yh}}{h}$. Since ϕ is a constant, we can do the same integration for the vertical direction combined with horizontal magnetic component:

$$\dot{y}(z) = \frac{\kappa}{\gamma} \sum_h b_{xh} \sin\left(\frac{2\pi h}{\lambda_u} z + \phi\right) \tag{A.6}$$

In our case for ultra-relativistic electrons, we apply an important approximation: The horizontal normalised speed β_x is evaluated as equal to $\dot{x}$:

$$\dot{x}(z) = \frac{dx}{dz} \approx \frac{1}{c}\frac{dx}{dt} = \beta_x \tag{A.7}$$

Though we are actually interested in the longitudinal component:

$$\beta_z^2 = \beta^2 - \left(\beta_x^2 + \beta_y^2\right) \tag{A.8}$$

And since β_x and $\beta_y \ll \beta$ (or β_z), we are able to use the equivalent infinitesimal: $(1+x)^{\frac{1}{2}} \sim 1 + \frac{x}{2}$, Eq. (A.8) is approximated to be:

$$\beta_z = \beta\sqrt{1 - \frac{\beta_x^2 + \beta_y^2}{\beta^2}} \approx \beta\left(1 - \frac{\beta_x^2 + \beta_y^2}{2\beta^2}\right) \tag{A.9}$$

Now let us simplify the expression of β^2, first for x direction. Extending equation (A.5) with (A.7), we get:

$$\beta_x^2 = \frac{\kappa^2}{\gamma^2} \sum_h \sum_{h'} b_{yh} b_{yh'} \sin\left(\frac{2\pi h}{\lambda_u} z\right) \sin\left(\frac{2\pi h'}{\lambda_u} z\right) \tag{A.10}$$

In one undulator period λ_u, the integral sine products from different harmonics equal to zero:

$$\langle \sin(ax)\sin(bx)\rangle = 0, \quad \text{if} \quad |a| \neq |b| \quad \text{and} \quad a, b \in Z$$

As a consequence, Eq. (A.10) can be integrated and simplified as:

$$\begin{aligned}\langle \beta_x^2 \rangle &= \frac{1}{\lambda_u}\int_0^{\lambda_u} \frac{\kappa^2}{\gamma^2} \sum_h b_{yh}^2 \sin^2\left(\frac{2\pi h}{\lambda_u} z\right) \mathrm{d}z \\ &= \frac{\kappa^2}{2\gamma^2} \sum_h b_{yh}^2\end{aligned} \tag{A.11}$$

Considering that in one period λ_u, the constant phase difference ϕ does not change the integration, we can calculate for y direction in the same way and obtain $\langle \beta_y^2 \rangle$ from Eq. (A.6):

$$\begin{aligned}\langle \beta_y^2 \rangle &= \frac{1}{\lambda_u}\int_0^{\lambda_u} \frac{\kappa^2}{\gamma^2} \sum_h b_{xh}^2 \sin^2\left(\frac{2\pi h}{\lambda_u} z + \phi\right) \mathrm{d}z \\ &= \frac{\kappa^2}{2\gamma^2} \sum_h b_{xh}^2\end{aligned} \tag{A.12}$$

Now we can extend the expression of $\langle \beta_z \rangle$ by combining Eqs. (A.11) and (A.12) within Eq. (A.9):

$$\begin{aligned}\langle \beta_z \rangle &= \beta\left(1 - \frac{\langle \beta_x^2 \rangle + \langle \beta_y^2 \rangle}{2\beta^2}\right) \\ &= \beta\left(1 - \frac{\kappa^2}{4\beta^2\gamma^2} \sum_h \left(b_{yh}^2 + b_{xh}^2\right)\right)\end{aligned} \tag{A.13}$$

Applying again the approximation with equivalent infinitesimal: $\beta = \sqrt{1-\frac{1}{\gamma^2}} \approx 1 - \frac{1}{2\gamma^2}$, Eq. (A.13) becomes:

$$\langle \beta_z \rangle = 1 - \frac{1}{2\gamma^2} - \frac{\kappa^2}{4\beta\gamma^2} \sum_h \left(b_{yh}^2 + b_{xh}^2 \right) \tag{A.14}$$

Now we introduce the resonance condition [15]:

$$p\lambda_r = \frac{\lambda_u}{\langle \beta_z \rangle} - \lambda_u = \lambda_u \left(\langle \beta_z \rangle^{-1} - 1 \right)$$

where p is a positive integer, λ the radiation wavelength and λ_u the undulator period. Combining with Eq. (A.14), we obtain:

$$p\lambda_r = \lambda_u \left(\frac{1}{2\gamma^2} + \frac{\kappa^2}{4\beta\gamma^2} \sum_h \left(b_{yh}^2 + b_{xh}^2 \right) \right), p \in N^* \tag{A.15}$$

The undulator associated deflection parameter is defined as $K = \frac{e\lambda_u}{2\pi mc} B = \kappa B$. In our case, we can define an effective value of K to get the relation between λ and B, which is useful for another purpose.

$$K = \kappa \sqrt{\sum_h \left(b_{yh}^2 + b_{xh}^2 \right)} \tag{A.16}$$

where $\boldsymbol{b}_h = (b_{xh}, b_{yh}) = \boldsymbol{B}_h / h$.

A.2. Prediction of the deflection parameter of APPLE X in elliptical polarisation

We are able to do the calculation directly in the complex domain. With a definition in form of vector:

$$\hat{\boldsymbol{K}}_h = \kappa \frac{\hat{\boldsymbol{B}}_h}{h} = \kappa \hat{\boldsymbol{b}}_h$$

The Eq. (A.16) changes as:

$$K^2 = \sum_h \hat{\boldsymbol{K}}_h \cdot \hat{\boldsymbol{K}}_h^* \tag{A.17}$$

The change from $\boldsymbol{b} = \begin{pmatrix} b_x \\ b_y \end{pmatrix}$ in z (spatial) domain to $\hat{\boldsymbol{b}} = \begin{pmatrix} \hat{b}_x \\ \hat{b}_y \end{pmatrix}$ in ω (complex) domain:

$$b_x^2 + b_y^2 = \boldsymbol{b}^T \cdot \boldsymbol{b} = \hat{b}_x \cdot \hat{b}_x^* + \hat{b}_y \cdot \hat{b}_y^* = \hat{\boldsymbol{b}}^T \cdot \hat{\boldsymbol{b}}^*$$

Combining Eqs. (8) and (A.17), we obtain the equation of K:

$$K = \kappa \sqrt{\sum_h \left(\sum_{n=1}^{4} e^{ih\varphi_n} \boldsymbol{R}_n \cdot \hat{\boldsymbol{b}}_{1h} \right)^T \cdot \left(\sum_{n=1}^{4} e^{ih\varphi_n} \boldsymbol{R}_n \cdot \hat{\boldsymbol{b}}_{1h} \right)^*} \tag{A.18}$$

The $\boldsymbol{Z}$ matrix is introduced as a combination of the rotation matrix and the longitudinal shifts, whose definition is:

$$Z_{xh} = e^{ih\varphi_1} - e^{ih\varphi_2} + e^{ih\varphi_3} - e^{ih\varphi_4}$$
$$Z_{yh} = e^{ih\varphi_1} + e^{ih\varphi_2} + e^{ih\varphi_3} + e^{ih\varphi_4}$$
$$\boldsymbol{Z}_h = \begin{bmatrix} Z_{xh} & 0 \\ 0 & Z_{yh} \end{bmatrix}$$

Then the Eq. (A.18) becomes:

$$K = \kappa \sqrt{\sum_h \left(\boldsymbol{Z}_h \cdot \hat{\boldsymbol{b}}_{1h} \right)^T \cdot \left(\boldsymbol{Z}_h \cdot \hat{\boldsymbol{b}}_{1h} \right)^*} \tag{A.19}$$

To change the elliptical polarisation state, we shift relatively arrays No.1 and No.3 in the same direction. The relative phase shift differences of the arrays vary thus in this way:

$$\varphi_1 = \phi_p, \quad \varphi_2 = 0, \quad \varphi_3 = \phi_p, \quad \varphi_4 = 0$$

With the $\boldsymbol{Z}_h$ matrix, the number of the array does not play a role anymore, we can note b_{1h} as b_h. We obtain then K in *parallel operational mode*:

$$K(\phi_p) = 2\sqrt{2}\kappa \sqrt{\sum_h (b_{xh}^2 + b_{yh}^2) - \cos(h\phi_p)(b_{xh}^2 - b_{yh}^2)} \tag{A.20}$$

Because of the symmetry of the APPLE X undulators, the horizontal and the vertical magnetic field components are equal: $\hat{B}_h = \hat{B}_{1h} = \hat{B}_{1xh} = \hat{B}_{1yh}$, the Eq. (A.20) becomes:

$$K = 4\kappa \sqrt{\sum_h \left(\frac{\hat{B}_h}{h} \right)^2}. \tag{A.21}$$

References

[1] C.J. Milne, T. Schietinger, M. Aiba, A. Alarcon, J. Alex, A. Anghel, V. Arsov, C. Beard, P. Beaud, S. Bettoni, et al., Swissfel: the swiss x-ray free electron laser, Appl. Sci. 7 (7) (2017) 720.

[2] R. Abela, A. Alarcon, J. Alex, C. Arrell, V. Arsov, S. Bettoni, M. Bopp, C. Bostedt, H.-H. Braun, M. Calvi, et al., The swissfel soft X-ray free-electron laser beamline: Athos, J. Synchrotron Radiat. 26 (4) (2019).

[3] T. Schmidt, M. Calvi, APPLE X undulator for the swissfel soft X-ray beamline athos, Synchrotron Radiat. News 31 (3) (2018) 35–40.

[4] R. Carr, Adjustable phase insertion devices as x-ray sources, Nucl. Instrum. Methods Phys. Res. A 306 (1991) 391–396.

[5] S. Sasaki, Design of a new type of planar undulator for generating variably polarized radiation, Nucl. Instrum. Methods Phys. Res. A 331 (1–3) (1993) 763–767.

[6] P. Elleaume, Helios: a new type of linear/helical undulator, J. Synchrotron Radiat. 1 (1994) 19–26.

[7] S. Sasaki, K. Kakuno, T. Takada, T. Shimada, Y. Yanagida, Analyses for a planar variably-polarizing undulator, Nucl. Instrum. Methods Phys. Res. A 347 (1–3) (1994) 83.

[8] J. Bahrdt, W. Frentrup, A. Gaupp, B. Kuske, A. Meseck, M. Scheer, Undulators for the bessy sase-fel project, in: AIP Conf. Proc., Vol. 705, 2004, pp. 215–218.

[9] T. Schmidt, A. Imhof, G. Ingold, B. Jakob, C. Vollenweider, Undulators for the bessy sase-fel project, in: AIP Conf. Proc., Vol. 879, 2007, pp. 400–403.

[10] A.B. Temnykh, Delta undulator for Cornell energy recovery linac, Phys. Rev. ST Accel. Beams 11 (120702) (2008) 10.

[11] M. Calvi, C. Camenzuli, E. Prat, T. Schmidt, Transverse gradient in apple-type undulators, J. Synchrotron Radiat. 24 (3) (2017) 600–608.

[12] A. Temnykh, M. Babzien, D. Davis, M. Fedurin, K. Kusche, J. Park, V. Yakimenko, Delta undulator model: Magnetic field and beam test results, Nucl. Instrum. Methods Phys. Res. A 649 (1) (2011) 42–45.

[13] G. Martinek, U. Wyss, D. Maybury, S. Constantinides, Optimizing magnetic effects through shaped field magnets, in: Proceeding of the 6th International Conference on Magnetism and Metallurgy, Cardiff, 2014.

[14] X. Liang, M. Calvi, C. Kittel, N. Sammut, T. Schmidt, Advanced operational models of the apple x undulator, in: 39th Free Electron Laser Conf.(FEL'19), Hamburg, Germany, 26-30 August 2019, JACOW Publishing, Geneva, Switzerland, 2019, pp. 541–544.

[15] J.A. Clarke, The Science and Technology of Undulators and Wigglers, Vol. 4, Oxford University Press on Demand, 2004.

[16] P. Elleaume, O. Chubar, J. Chavanne, Computing 3d magnetic fields from insertion devices, in: Proceedings of the 1997 Particle Accelerator Conference (Cat. No. 97CH36167), Vol. 3, IEEE, 1997, pp. 3509–3511.

[17] O. Chubar, P. Elleaume, J. Chavanne, A 3d magnetostatics computer code for insertion devices, sri97 conf. aug. 1997, J. Synchrotron Radiat. 5 (1998) 481–484.

[18] J. Cassar, A. Sammut, N. Sammut, M. Calvi, Z. Mitrovic, R.S. Popovic, Calibration and characterization of a reduced form-factor high accuracy three-axis teslameter, Electronics 9 (1) (2020) pp. 18.

[19] J. Cassar, A. Sammut, N. Sammut, M. Calvi, S. Dimitrijevic, R.S. Popovic, Design and development of a reduced form-factor high accuracy three-axis teslameter, Electronics 8 (3) (2019) pp. 21.

[20] J. Cassar, A. Sammut, N. Sammut, M. Calvi, S. Spasic, D.P. Renella, Performance analysis of a reduced form-factor high accuracy three-axis teslameter, Electronics 8 (11) (2020) pp. 18.

[21] T. Tanaka, R. Tsuru, T. Nakajima, H. Kitamura, Magnetic characterization for cryogenic permanent-magnet undulators: a first result, J. Synchrotron Radiat. 14 (2007) 416–420.

[22] M. Calvi, C. Camenzuli, R. Ganter, N. Sammut, T. Schmidt, Magnetic assessment and modelling of the aramis undulator beamline, J. Synchrotron Radiat. 25 (3) (2018) 686–705.

[23] R.S. Popovic, Hall Effect Devices, CRC Press, 2003.